

Polymeric Nano-Blue-Energy Generator Based on Anion-Selective Ionomers with 3D Pores and pH-Driving Gating

Xuanbo Zhu, Jundong Zhong, Junran Hao, Yuzhang Wang, Jiajia Zhou, Jingwen Liao, Yujie Dong, Jinhui Pang, Haibo Zhang, Zizhun Wang, Wei Zhang, Weitao Zheng, Zhenhua Jiang, Yahong Zhou,* and Lei Jiang

Blue energy as a renewable, substantial energy resource has attracted scientists who are interested in discovering abundant membrane materials to achieve high power density. For decades, ionomers have been used as ion-exchange membrane to harvest this energy. Though extensive studies have been conducted, the underlying mechanism of ionic transmembrane behavior is still under debate. Here, the ionic transmembrane properties through membranes with 3D pores prepared by ionomers (polyphenylsulphone with pyridine pendants (PPSU-Py)) are systematically studied. A series of PPSU-Py with tunable porosities and surface charge densities is obtained simply by adjusting the percentages of the pendant. Nanoscale morphologies of the ionomers are simulated with the dissipative particle dynamic method, which is in agreement with the experimental data. Then, nanofluidic behaviors of as-prepared porous membranes are studied, which exhibit anion selectivity, pH gating, and modulated transmembrane conductance. Furthermore, a series of salinity gradient power harvesters based on the ionomers are constructed, of which the output power density is improved by tuning the charge density with the maximum output power density that reaches up to 1.44 W m^{-2} . The impact of the ionomer on nanofluidic behavior is systematically discussed, and it is believed this work will shed light on nanofluidic materials and blue energy generator design.

(RED), in particular, is an efficient approach to directly convert the osmotic power between the sea water and river water into electric current.^[1–4] Though decades have passed, the nanofluidic system that determines the RED approach process raises fundamental issues about the impact of surface charge on ionic transmembrane property.^[5–8] Developments in nanomanufacturing have triggered technological revolutions in nanoporous membrane design and fabrication.^[4,9–15] Selecting porous membranes is of the essence for the design of said energy devices. So far, inorganic composite, organic materials, soft matter hydrogel,^[16] wood,^[17] silk,^[18,19] etc.^[20–25] have been used to harness salinity gradient energy and have made a giant leap for the applications. Advanced polymers, especially functional ionomers, hold great potential in nanofluid devices because of their unique ion selectivity, uniform 3D pore structure, and physical mechanical properties.^[26–28] Ionomers with available chemical diversity could self-assemble into 3D pores

1. Introduction

Blue energy has drawn much attention in recent years because of its clean and sustainable properties. Reverse electrodialysis

by intermolecular phase separation, which bear hydrophilic functional ionic pendants and hydrophobic backbone.^[26–29] For decades, ionomers are extensively used as solid electrolytes in electrochemical technologies, especially serving as the

Dr. X. Zhu, Dr. J. Zhong, Prof. J. Pang, Prof. H. Zhang, Prof. Z. Jiang
National and Local Joint Engineering Laboratory for Synthetic
Technology of High Performance Polymer
College of Chemistry
Jilin University
Changchun, Jilin 130012, P. R. China

J. Hao, Dr. Y. Zhou, Prof. L. Jiang
CAS Key Laboratory of Bio-inspired Materials and Interfacial Science
Technical Institute of Physics and Chemistry
Chinese Academy of Sciences
Beijing 100190, P. R. China
E-mail: zhoyh@mail.ipc.ac.cn

J. Hao, Y. Wang, Prof. J. Zhou, Prof. L. Jiang
Beijing Advanced Innovation Center for Biomedical Engineering
Beihang University
Beijing 100191, P. R. China

Dr. J. Liao
Guangzhou Institute of Advanced Technology
Chinese Academy of Sciences
Guangzhou, Guangdong 511458, P. R. China

Dr. Y. Dong
State Key Laboratory Breeding Base of Green Chemistry Synthesis
Technology
College of Chemical Engineering
Zhejiang University of Technology
Hangzhou, Zhejiang 310014, P. R. China

Dr. Z. Wang, Prof. W. Zhang, Prof. W. Zheng
State Key Laboratory of Automotive Simulation and Control
School of Materials Science and Engineering
Electron Microscopy Center, International Center of Future Science
Jilin University
Changchun, Jilin 130012, P. R. China

 The ORCID identification number(s) for the author(s) of this article can be found under <https://doi.org/10.1002/aenm.202001552>.

DOI: 10.1002/aenm.202001552

proton-exchange membrane.^[30] For example, Nafion is still used as a cation-selective membrane in fuel cells since 1970s.^[31,32] With regards to ionic transport mechanism, ion-hopping model has long been dominating in the explanation of proton transport.^[33,34] On this basis, several morphological models have been proposed for the ionic transport mechanism, such as cluster-network model,^[31,35] rod-like polymer structure,^[36] parallel-cylindrical water channels^[27] model, and bicontinuous network of ionic clusters.^[37] Recently, with developments in nanotechnology and theoretical simulations, 3D interconnected pores model induced by the intermolecular interaction is commonly accepted.^[27] It had been proved that this channels theory existed in organic electrolyte and the phenomena are proved by simulation data.^[29,38] The electric field generated by the charges along the channels facilitates opposite charged ions to move through the pore while defer the entry of the same charged ions. Compared to the ion-hopping mechanism,^[39] referring to the specific interaction between the proton and charged groups, this nanofluidic theory obeys the electric-field effect theory in ultraconfined environment (including double electric layer, Poisson distribution, and steady-state Nernst–Planck).^[7]

Ionic transmembrane behavior^[40] across the interface between the electrolyte and pores determines the energy conversion process and is a fundamental issue involving the chemical and physical processes.^[41] Generally, this ion transport property is observed in the artificial porous membrane tailoring pore surface chemistries or pore geometries. Compared to solvent phase separation-induced polymeric porous membrane, structural control at the molecular level reduces diversity in the nanoscale morphologies and provides a powerful approach to fabricate membrane with uniform 3D pores and tunable porosity. Porous membrane with tunable porosity and uniform 3D pores is an ideal model to study the ionic transmembrane behavior across the interface between electrolytes and pores.

In this article, we have designed a series of advanced polymer polyphenylsulphone with pyridine (PPSU-Py_x) to promote ion-selective transport with improved mechanical properties,

and then explore it as blue energy generator candidate. At the molecular level, uniform 3D porous membranes with a wide range of porosity from 2.2% to 13.8% are successfully prepared through simple self-assembly approach (Figure 1A). Surface charge density is a key factor that impacts the ionic transmembrane properties, so here we modulate the surface charge density by tuning the pendant proportion through exquisite chemical polymerization design (Figure S1, Supporting Information). The ionic transmembrane conductance increases more than threefold, and the membrane shows reversible pH-induced gating properties due to the pyridine group along the pores (Figure 1B). Furthermore, we simulated the pore structure in the membrane by dissipative particle dynamic (DPD) (Figure 1C). The as-prepared membrane is then constructed as salinity gradient power generators (Figure 1D,E) and the maximum output power density is 1.44 W m⁻². Developing nanoporous materials with tunable charge density and porosity that respond to external stimuli could provide fundamental insights into the links between the molecular design and ionic transmembrane properties.

2. Results and Discussion

2.1. Preparing the 3D Porous Membrane

A series of copolymer polyphenylsulphone pyridine with pyridine proportion ranging from 20% to 100% was copolymerized by fine-chemical synthesis during the nucleophilic substitution reaction (Schemes S1 and S2, Supporting Information). This polymerization process is confirmed by the ¹H NMR (Figures S2 and S3, Supporting Information). The membrane was simply prepared by pouring PPSU-Py solution onto leveled clean glass plates after filtration. The thickness of copolymer membrane was imaged using scanning electron microscopy (SEM). The sample was prepared by frozen-cracking to give an accurate picture. The cross section shows the membrane is ≈7 μm in thickness.

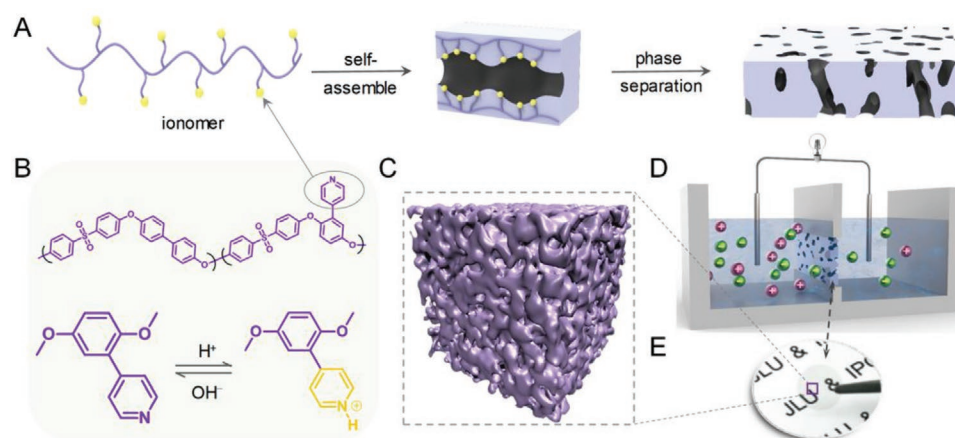


Figure 1. Schematic depiction of 3D porous PPSU-Py membrane. A) The ionomer self-assembles into 3D pores via phase separation process. B) Chemical composition and pH-responsiveness of PPSU-Py. The pyridine group can be protonated to form Py-H⁺ in the acidic environment. Conversely, Py-H⁺ can be deprotonated in the alkaline environment. Thus, charge density in the membrane can be charged by varying the pH of the external environment. C) The typical 3D phase diagram of PPSU-Py membrane (hydrophobic chain is purple) performed DPD simulation. D) Cartoon illustration of PPSU-Py membrane-based energy-collecting device. The membrane is mounted in a two-compartment electrochemical cell to collect osmotic energy from a concentration gradient. E) Digital photograph of the macroscopic membrane with an approximate thickness of 7 μm.

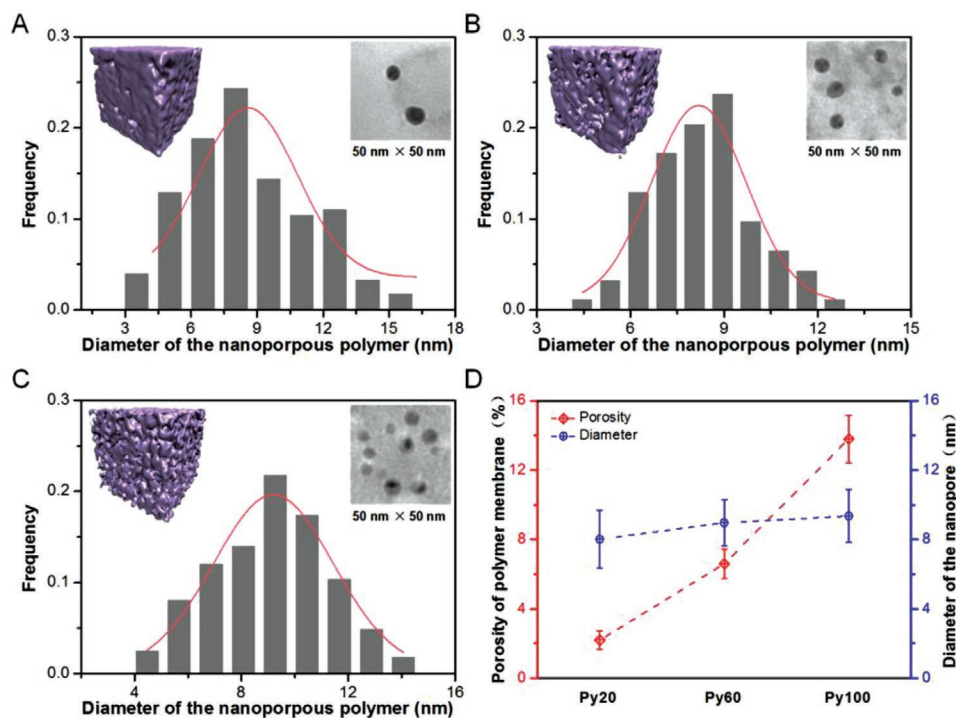


Figure 2. The microscopic pore structure characterization and size statistical result of PPSU-Py with tuning pyridine pendant proportion. A–C) The histogram of pore size distribution with Gaussian fit of the pore size distribution according to the TEM images of Py20, Py60, and Py100, respectively. Insets in the left are 3D phase diagram of PPSU-Py membranes. Insets in the right are the 50 nm × 50 nm partial TEM images of the polymer membrane marked with PTA. Dark areas refer to pores formed by the pyridine groups. The white areas refer to the hydrophobic backbone domains. All samples display uniform rounded pores randomly distributed on the membrane surface. According to these TEM images, the diameters of the copolymer membranes can be read and counted (Figure 2A–C). Using ImageJ software, porosity (the ratio of total dark area to the total membrane area) analyses were performed. Clearly, the pore size of all membranes read in the TEM images is basically the same, and the diameters of the three membranes are 8.1, 8.9, and 9.3 nm, respectively. Meanwhile, the porosity of the membranes is 2.2%, 6.6%, and 13.8%, respectively. With the increasing proportion of pyridine group, the porosity increased more than six fold. These almost the same-sized pores are mainly attributed to the intramolecular interactions inside the amphiphilic copolymer. The pores in ionomer generated by the intermolecular interaction tend to be spherical. The TEM exhibits the morphology of the pore within several nanometers of thickness. Beneath it, the same spherical pores overlapped each other. Thus, the 3D-networked channels would be formed in the membrane.

2.2. Nanoscale Morphologies of 3D Channels

The nanoscale morphologies of Py20, Py60, and Py100 were investigated by transmission electron microscopy (TEM) (upper-right insets of Figure 2A–C). To give a clear contrast between the pyridine domains and the hydrophobic backbone, the membranes were stained with phosphotungstic acid (PTA). It can mark the pores formed by the hydrophilic pyridine groups as dark areas. The white areas refer to the hydrophobic backbone domains. All samples display uniform rounded pores randomly distributed on the membrane surface. According to these TEM images, the diameters of the copolymer membranes can be read and counted (Figure 2A–C). Using ImageJ software, porosity (the ratio of total dark area to the total membrane area) analyses were performed. Clearly, the pore size of all membranes read in the TEM images is basically the same, and the diameters of the three membranes are 8.1, 8.9, and 9.3 nm, respectively. Meanwhile, the porosity of the membranes is 2.2%, 6.6%, and 13.8%, respectively. With the increasing proportion of pyridine group, the porosity increased more than six fold. These almost the same-sized pores are mainly attributed to the intramolecular interactions inside the amphiphilic copolymer. The pores in ionomer generated by the intermolecular interaction tend to be spherical. The TEM exhibits the morphology of the pore within several nanometers of thickness. Beneath it, the same spherical pores overlapped each other. Thus, the 3D-networked channels would be formed in the membrane.

To confirm this pore structure, nitrogen adsorption–desorption (BET) was employed to analyze the pore size distribution of the prepared membranes (Figure S4, Supporting Information). It is similar to the results obtained by TEM image analysis. Also we furthermore simulated the phase morphologies of the membranes using DPD method that is a coarse grained simulation method.^[42–44] The interactions between the particles are governed by the following forces: conservative force, dissipative force, and random force.^[45–47] The upper-left insets in Figure 2 are periodic 3D images of PPSU-Pyx membranes, and all the images display interconnected hydrophilic channels (hydrophobic chain is purple). Significantly, as the proportion of the charged pendant increases, the channels become denser. These morphologies are consistent with our analysis and the TEM images. Besides, these simulation data proved that the porosity of the membrane increases with increase in the pyridine proportion, which is in accord with the TEM images as well. So, we obtained nanoporous membrane with controlled porosity and uniform pore size by modulating the pendant proportion of the ionomers.

2.3. Nanofluidic Behavior of the Membrane

The nanofluidic behavior of the membrane across the interface between the solution and porous membrane plays a fundamental role in the osmotic energy conversion process. To better

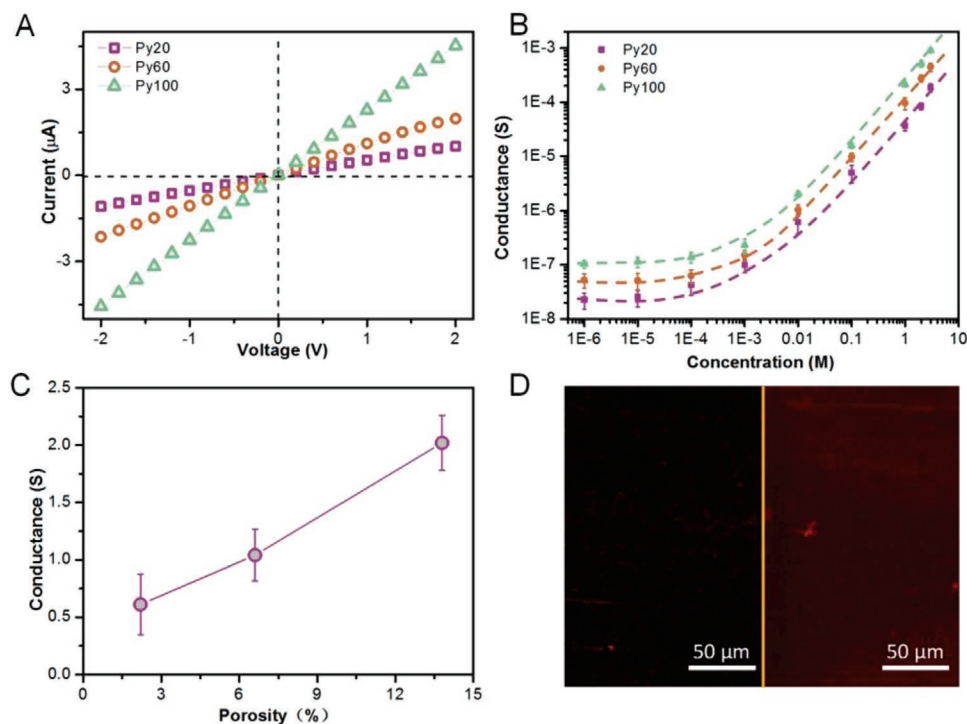


Figure 3. The ionic transmembrane conductance with increasing porosity, and selectivity property. A) I - V curves of the nanoporous membrane in 0.01 M KCl solution with pH 6.0. B) Conductance versus salt concentration for a series of copolymer PPSU, with pH 6.0. Conductance of membranes with a series of KCl concentration at pH 6 and shows deviations at low concentrations, demonstrating the effect of surface charge on the ionic transport. C) Conductance as a function of porosity in 0.01 M KCl solution at pH 6, for Py20 (2.2%), Py60 (6.6%), and Py100 (13.8%), and shows an approximate linear relationship. D) The CLSM images of the membrane with positively charged fluorescent dye (left) and negatively charged fluorescent dye (right). The dye molecule with negative charge could pass through while the positively charged dyes are repelled, the membrane behaving as an anion selector.

understand the performance of the nanochannels in the membranes, ionic transmembrane transport properties are measured using electrochemical method. The copolymer membrane was fixed at the junction of a two-compartment electrochemical cell as a separator. The current–voltage (I - V) response of the nanochannel was characterized by a pair of Ag|AgCl electrodes. Sweeping voltages from -2 to 2 V were applied across the membrane with the step voltage of 200 mV. From the I - V curves (all recorded in 0.01 M KCl solution) of Py20, Py60, and Py100, the conductance increased significantly with the increased proportion of pyridine (Figure 3A). This result also testified the TEM images. The linear current without ionic current rectification indicates that the 3D pore structures inside the membrane are symmetric.

2.4. Transmembrane Ionic Conductance

2.4.1. Surface Charge and Porosity Determines the Ionic Conductance

From Py20 to Py100, the porosity increased more than sixfold while the conductance of Py100 is about 4.5 times that of Py20. Compared to the curves of conductance versus concentration with single channels, the ionic transport is highly dependent on the ionic concentration as well. At low concentrations, the ionic conductance deviates from bulk value and gradually turns and

shows saturation (Figure 3B), suggesting a sign of the presence of surface charge on the pores. For the single pore, the conductance in dilute solution is independent of the pore size.^[6] However, for this multi-3D-porous membrane, the conductance shows high dependence on the porosity as well both in high and low salt concentration. The change of transmembrane ionic conductance originates from the porosity of membrane (Figure 3C). To gain insight into the ion transport mechanism, a numerical simulation based on the Poisson and Nernst–Planck (PNP) equations was performed (Figures S5 and S6, Supporting Information). As can be seen, for PPSU-Py membranes, ionic transport performance is dominated by the charged pore wall in long nanochannels, and the impact of pore–pore interaction is limited.^[48,49] So the response of conductance with increasing porosities shows an approximate linear relationship. This gives us a sign that by chemical molecular design, porous membrane with modulated porosity could be obtained that has much impact on the nanofluidic behavior.^[38]

2.5. Selectivity of the Membrane

Generally, the charged nanoporous membrane holds ionic selectivity property. The PPSU membrane contains positive charge (Py- H^+) in the acidic environment. To testify the selectivity, we conducted a visual experiment for the selectivity that is performed by the confocal laser scanning microscope (CLSM).

Two oppositely charged fluorescent dyes are used to study the ionic selectivity. Sulfonated rhodamine, a negatively charged fluorescent dye molecule with high photostability, was selected. Propidium iodide was selected as the oppositely, positively charged fluorescent dye. A droplet of fluorescent dye solution is added onto the membrane from only one side. The CLSM is used to image the permeation of the fluorescent dyes through the membrane at the other side. As can be seen, only the negatively charged dyes are permeable across the membrane easily. The positively charged dyes are excluded from the membrane and cannot pass through (Figure 3D). These results confirmed that the membrane is anion-selective due to the positive surface charge from pyridine group and the narrow confined pores.^[50] In addition, the selectivity of the membrane is quantified in terms of transference number.^[51] It was tested by measuring the scanning I - V curves of PPSU-Pyx membranes under artificial seawater (0.5 m NaCl) and artificial river water (0.01 m NaCl). The equivalent circuit of the testing system is shown in Figure S7, Supporting Information. According to the experimental results (Table S3, Supporting Information), in the salinity gradient, based on asymmetric seawater and river water, Py20, Py60, and Py100 showed high ionic selectivity, and with the increasing of functional groups, the membrane showed better selectivity and the t_n of Py100 was up to 0.773. This highly efficient selectivity would benefit the energy conversion process.

2.6. pH Gating Property of the 3D Porous Membrane

Due to the functional charged group along the ionomer, the porous membrane may respond to the environment that is behaving as gatekeepers.^[38,52,53] The pyridine group bears positive charge and is sensitive to acid-base stimulation. Modulating the pH condition of the solution, both the surface charge density and wettability of the membrane are changed. Here, we examined the effect of pH on ionic transport by testing I - V curves with 0.01 m KCl (Figure 4). With the pH value varying from 11 to 3, the conductance increased almost tenfold. All the membranes in this series exhibit similar properties. The ionic nanogate “open” in the acidic environment and turns “off” in the alkaline environment. These results are mainly due to the pyridine pendant. In the acidic environment, the pyridine group is protonated to form Py-H^+ , so the channel is positive charged and hydrophilic. In this case, the high conductance (“OPEN” state) is obtained. Conversely, in the alkaline

environment, the Py-H^+ was replaced by uncharged pyridine group, the channel from positively charged to uncharged and hydrophobic, a sharp decline in conductance was obtained (“off” state). Also, the smart pH-driven ionic gating property has a favorable stability and reversibility. The cycling performance can be actualized by varying the pH value from 3 to 11 over and over again. As shown in Figure 4C, the transmembrane ionic current decreased obviously to around 1.1 μA (down) under pH 11. When the pH value is adjusted to 3, most pyridine group is protonated and converted to Py-H^+ . The transmembrane ionic current dramatically increased to around 10.6 μA (up). After several cycles, the current in the acidic environment is also about ten times higher than that in the alkaline environment. There was no obvious change in the current of the test sample. As shown in Figure 4, the membrane exhibited outstanding smart pH-driven ionic gating property and stabilized responsive switchability. This pH-driven ionic gating property proved the ionic transmembrane property is dependent on the surface charge and wettability.

2.7. Blue Energy Generator

Since this kind of membrane has anion selectivity that renders the membrane works as the salinity gradient energy harvester, we construct a blue energy generator based on such porous membranes bioinspired by the electric eel.^[54,55] The presence of the positive charge (Py-H^+) along the pores would screen the passing negative ions (Cl^-), and then a net current would be measured under a salinity gradient. Here, a chemical potential gradient system is introduced with salt (NaCl) concentration gradient system. The as-prepared membrane was fixed between the artificial seawater (0.5 m NaCl) and artificial river water (0.01 m NaCl) as a separator, and an energy-collecting generator is then built. Then, this collected power could be transferred to external circuit and supply an electronic load. As is well known to all, the maximum extractable power appears when the ionic internal resistance of the membrane is equal to the external load resistance.^[8,56] The power density of the resistor in the circuit is calculated with the equation $P = I^2R$. The output power and current density of membranes under a series of external load resistance are demonstrated in Figure 5A–C. Obviously, the current density is gradually reduced with the increasing load resistance. The output power reaches a maximum value at about 30, 20, and 15 $\text{k}\Omega$, respectively. At the lowest internal

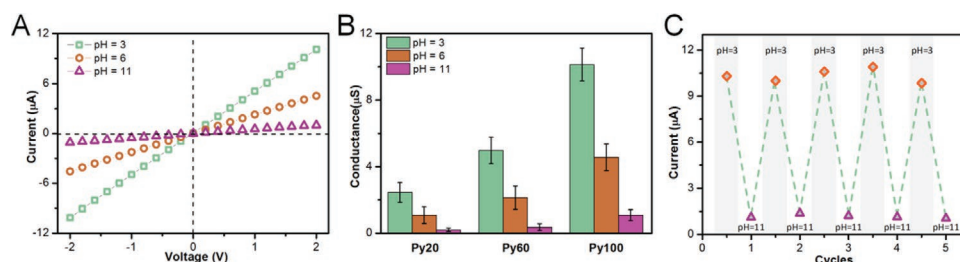


Figure 4. Ionic nanogate property of the membranes in response to environment. A) I - V curves of Py100 under 0.01 m KCl solution (pH = 3, 6, and 11) with a sweep voltage ranging from -2.0 to 2.0 V. B) The ionic conductance of the membranes in 0.01 m KCl solution with different pH values. A sharp decrease in conductance was obtained when varying the pH value from 3 to 11, indicating the ionic nanogate was “open” in the acidic environment and “off” in the alkaline environment. C) Responsive switchability of the pH-driven ionic nanogate. The reversible variation of the ionic current is measured alternately at 2 V with pH = 3 and 11.

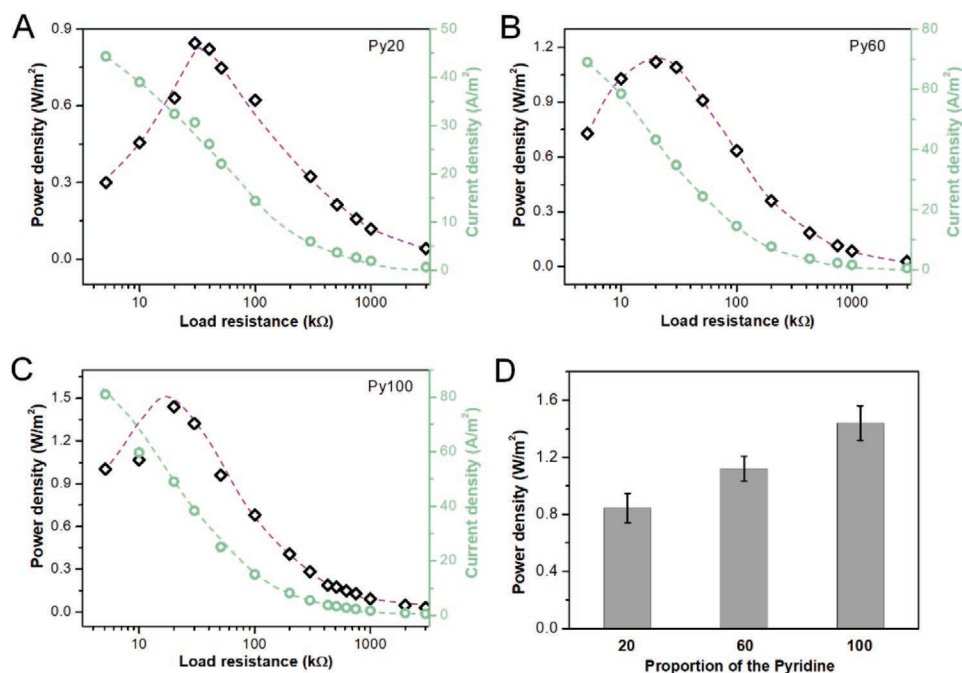


Figure 5. Application for harvesting osmotic power as a nanogenerator. Due to the ionic selectivity, a concentration-gradient-driven energy harvesting device was built. The copolymer membrane was fixed between the artificial seawater (0.5 M NaCl) and artificial river water (0.01 M NaCl) as a separator. The collected power is transferred to a resistor via an external circuit. A–C). The output power and current density of the membrane under a series of external load resistance. As load resistance gradually increases, the current density is reduced while the output power reaches a maximum at about 30, 20, and 15 kΩ, respectively. D). With the increasing pyridine pendant proportion, the maximal output power density increases.

resistance, the maximal output power of the energy-collecting device based on Py100 reached up to 1.44 W m^{-2} .

Clearly, the internal resistance of the membranes read in Figure 5 revealed that it decreases with the growth pendant proportion. For example, the resistance value of the Py100 is only half of that of Py20, and this trend is consistent with the output power density as well. The output power of Py100 is about two times that of Py20. Therefore, this work directly proves that precise design of the ionomer chemical structure could lead to high-performance blue energy harvester construction. Here, we also want to emphasize that that charged pyridine variation during the copolymerization process results in both the surface density and porosity improvement.

3. Conclusion and Perspective

Developing nanoporous membrane science plays a fundamental role in numerous applications, such as nanofluidic devices, energy collector, biosensor, drug controller, and so on. Along these, the key is the mechanism of ions/molecular transmembrane properties that is nanofluidic. So far, novel nanofluidic behavior is long being expected to emerge that may spark nanotechnology breakthrough and hold huge potential application. From the point of material design, the cooperation between ultraconfinement and diversified surface property would lead to unique nanofluidic property. So here, from the advanced polymer design, a series of ionomers with tunable molecular structure are copolymerized. On this basis, the 3D porous membrane is obtained simply by self-assembly route.

The membrane-forming process is simple and can be used in large-scale production. Both experimental and simulation data reveal the modulated porosity and pore structures. We have predicted that the increasing surface charge and porosity would benefit the nanofluidic behavior and further improve the blue energy harvesting power density. The experimental results also confirmed this expectation. The constructed blue energy harvesters reach a maximum output power density of 1.44 W m^{-2} . Through this study, the profile of ionomer on nanofluidic behavior is systematically discussed. Here, we talk about how to select and design porous membrane. We believe this work would shed light on nanofluidic materials and blue energy generator design.

4. Experimental Section

Materials and Characterization Methods: The manufacturers of the materials and reagents discussed in this study are listed in the Supporting Information. The characterization of the copolymers PPSU-Py with different proportion pendants was conducted using a Bruker 510 spectrometer (500 MHz for ¹H) with CDCl₃ or DMSO-*d*₆ as the solvent. The internal reference was tetramethylsilane (TMS). Using an Ubbelohde viscometer, the inherent viscosity of PPSU-Pyx was measured with 0.1 g samples dissolved in 20 mL of NMP at 25 °C. The nanofluidic behavior of the membrane was measured by a Keithley 6487 picoammeter (Keithley Instruments, Cleveland, OH, USA). The nanoscale morphologies of the polymeric pore structures were investigated by transmission electron microscope (JEM 2100F; JEOL, Japan). The fluorescent images that the permeation of fluorescent dyes through the membrane were obtained using a Nikon C2 CLSM (Nikon Corp., Tokyo, Japan).

- [43] R. D. Groot, T. J. Madden, *J. Chem. Phys.* **1998**, *108*, 8713.
- [44] N. Li, C. Wang, S. Y. Lee, C. H. Park, Y. M. Lee, M. D. Guiver, *Angew. Chem., Int. Ed.* **2011**, *50*, 9158.
- [45] P. J. Hoogerbrugge, J. M. V. A. Koelman, *Europhys. Lett.* **1992**, *19*, 155.
- [46] J. M. V. A. Koelman, P. J. Hoogerbrugge, *Europhys. Lett.* **1993**, *21*, 363.
- [47] P. Español, P. Warren, *Europhys. Lett.* **1995**, *30*, 191.
- [48] L. Cao, Q. Wen, Y. Feng, D. Ji, H. Li, N. Li, L. Jiang, W. Guo, *Adv. Funct. Mater.* **2018**, *28*, 1804189.
- [49] J. Gao, X. Liu, Y. Jiang, L. Ding, L. Jiang, W. Guo, *Small* **2019**, *15*, 1804279.
- [50] J. Cervera, B. Schiedt, R. Neumann, S. Mafé, P. Ramírez, *J. Chem. Phys.* **2006**, *124*, 104706.
- [51] M. Nishizawa, V. P. Menon, C. R. Martin, *Science* **1995**, *268*, 700.
- [52] G. W. de Groot, M. G. Santonicola, K. Sugihara, T. Zambelli, E. Reimhult, J. Vörös, G. J. Vancso, *ACS Appl. Mater. Interfaces* **2013**, *5*, 1400.
- [53] E. Maza, J. S. Tuninetti, N. Politakos, W. Knoll, S. Moya, O. Azzaroni, *Phys. Chem. Chem. Phys.* **2015**, *17*, 29935.
- [54] T. B. H. Schroeder, A. Guha, A. Lamoureux, G. Vanrenterghem, D. Sept, M. Shtein, J. Yang, M. Mayer, *Nature* **2017**, *552*, 214.
- [55] J. R. Gallant, L. L. Traeger, J. D. Volkening, H. Moffett, P.-H. Chen, C. D. Novina, G. N. Phillips, R. Anand, G. B. Wells, M. Pinch, R. Güth, G. A. Unguez, J. S. Albert, H. H. Zakon, M. P. Samanta, M. R. Sussman, *Science* **2014**, *344*, 1522.
- [56] W. Guo, L. Cao, J. Xia, F. Q. Nie, W. Ma, J. Xue, Y. Song, D. Zhu, Y. Wang, L. Jiang, *Adv. Funct. Mater.* **2010**, *20*, 1339.

ADVANCED ENERGY MATERIALS

Supporting Information

for *Adv. Energy Mater.*, DOI: 10.1002/aenm.202001552

Polymeric Nano-Blue-Energy Generator Based on Anion-Selective Ionomers with 3D Pores and pH-Driving Gating

Xuanbo Zhu, Jundong Zhong, Junran Hao, Yuzhang Wang, Jiajia Zhou, Jingwen Liao, Yujie Dong, Jinhui Pang, Haibo Zhang, Zizhun Wang, Wei Zhang, Weitao Zheng, Zhenhua Jiang, Yahong Zhou, and Lei Jiang*

Supporting Information

Polymeric Nano-Blue-Energy Generator Based on Anion-Selective Ionomers with 3D Pores and pH-Driving Gating

Xuanbo Zhu, Jundong Zhong, Junran Hao, Yuzhang Wang, Jiajia Zhou, Jingwen Liao, Yujie Dong, Jinhui Pang, Haibo Zhang, Zizhun Wang, Wei Zhang, Weitao Zheng, Zhenhua Jiang, Yahong Zhou and Lei Jiang*

Content

- 1. Materials**
- 2. Measurements**
- 3. Zeta potential of PPSU-Py membrane**
- 4. Synthesis and characterization of co-polymer PPSU-Py**
 - 4.1 Synthesis of monomer**
 - 4.2 Characterization of monomer**
 - 4.3 Synthesis of polymer**
 - 4.4 Characterization of polymer**
- 5. Inherent viscosity of the copolymers**
- 6. Nitrogen adsorption-desorption**
- 7. Numerical simulation**
- 8. Ion selectivity and electrode calibration**
- 9. Thermal stability of PPSU-Pyx**
- 10. Experimental setup**

- 1. Materials**

Table S1. Experiment materials.

Material	Purity	Manufacturer
4, 4'-difluorodiphenyl sulfone	99%	Energy Chemical
4-pyridylboronic acid	98%	Energy Chemical
1-bromo-2,5-dimethoxybenzene	98%	Energy Chemical
borontribromide	99%	Energy Chemical
phosphotungstic acid	AR	Energy Chemical
tetrakis(triphenylphosphine)palladium (0)	99%	Energy Chemical
4, 4'-biphenol	99%	Honsyu Chemical Co. Ltd
tetramethylene sulfone	CP	Aladin Ltd

The above-mentioned reagents in Table S1 were used as received without any further purification. Other chemical reagents and organic solvents were purchased from Beijing Chemical Factory and were purified by conventional methods. All reagents are at least analytical grade. Anhydrous potassium carbonate (K_2CO_3) was dried at $120^\circ C$ for 24 h before polymerization reaction. Deionized water with a resistivity of $18.2 M\Omega cm^{-1}$ was obtained from the Milli-Q purification system (Millipore, Billerica, MA, USA).

2. Measurements

1H NMR experiments were conducted using a Bruker 510 spectrometer (500 MHz for 1H) with $CDCl_3$ or $DMSO-d_6$ as the solvent. The internal reference was tetramethylsilane (TMS). Using a Ubbelohde viscometer, the inherent viscosity of PPSU-Pyx was measured, with 0.1 g samples dissolved in 20 mL of DMAc at $25^\circ C$. The ionic current through the membrane was measured by a Keithley 6487 picoammeter (Keithley Instruments, Cleveland, OH). The cross section images of the sample were obtained with a field-emission scanning electron microscope (S-4800, Japan). The membranes were quenched with liquid nitrogen. The pore structure of the

copolymers was investigated by transmission electron microscope (JEM 2100F; Jeol, Japan). Diluted PPSU-Pyx solutions were cast on an ultrathin-carbon-coated copper grid. Selective staining of the pyridine was accomplished by exposure of the thin sections to phosphotungstic acid solution. The fluorescently images that the permeation of fluorescent dyes through the membrane from the perpendicular direction were obtained using a Nikon C2 confocal laser scanning microscope (Nikon Corp., Tokyo, Japan). The thermal stability was characterized by DSC Q2000 (TA Instruments, LLC, USA) and PerkinElmer Pyris 1 TGA apparatus (Waltham, Massachusetts, USA).

3. Zeta potential of PPSU-Py membrane

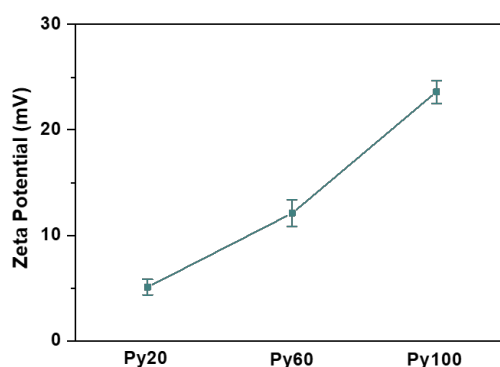


Figure S1. The Zeta potential of the membrane PPSU-Py20, PPSU-Py60 and PPSU-Py100 measured by SurPASS Electro-kinetic Analyzer (Anton-Paar) at pH=3. It means that the most pyridine groups can be protonated to form Py-H^+ , which can be used to describe the relationship between molecular structure and electric quantity more accurately. The surface charge density improves significantly with increasing pendant proportion.

4. Synthesis and Characterization of co-polymer PPSU-Py

We prepared a pyridine-containing hydroquinone monomer Py-OH by Suzuki

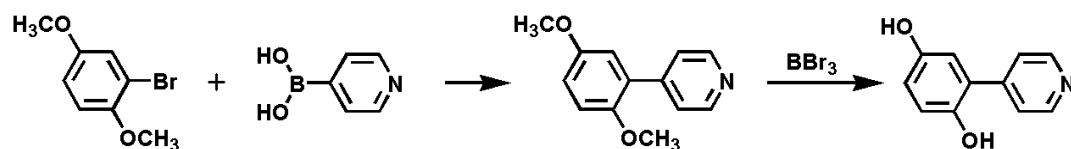
cross-coupling using 4-pyridylboronic acid. The nucleophilic terpolymerization of this monomer with biphenyldiol and difluorodiphenyl sulfone successfully introduced the pH-responsive group pyridine into Polyphenylene sulfone (PPSU), and by controlling the ratio of monomers, the synthesis of PPSU-Pyx with any pyridine proportions can be achieved.

4.1 Synthesis of monomer

As shown in Scheme S1, to connect pyridine to benzene ring, we built C-C bond through Suzuki cross-coupling, and used methoxyl group to protect phenol group, so as to prevent the influence of phenol hydroxyl.

Step 1:

The following reagents and solvents were put into a 250 mL round-bottom flask equipped with a stirring bar and a condenser: 10.85 g 1-Bromo-2,5-dimethoxybenzene, 9.22 g 4-pyridylboronic acid and 20 g K_2CO_3 . A mixed liquor of 120 ml 1,4-dioxane and 60 ml H_2O is used as solvent. Subsequently, the mixed reagents and solvent were degassed by the Schlenk Line with argon atmosphere. And then tetrakis(triphenylphosphine)palladium (0) (1.73 g) was added while the whole system was being purged in argon atmosphere. After the materials as prepared, the flask was heated up to $90^\circ C$ for 24 h with the agitation on. The proceeding degree of the reaction was ascertained with TLC (Thin-Layer Chromatography). At last, the reaction solution was cooled to room temperature, and a Rotary Evaporators removed the solvent. Purification was achieved by flash chromatography (tetrahydrofuran/petroleum ether) on silica gel. Catalyst can be removed simultaneously. Then our goal monomer 2-(pyridin-4-yl)-1,4-dimethoxybenzene (Py-OMe) was obtained after purification (9.68g, yield 90%).



Scheme S1. Synthesis of Py-OMe and Py-OH.

Step 2:

By using a dichloromethane solution of BBr_3 , dimethoxybenzene was demethylated to acquire the bisphenol monomer (Py-OH) as expected.

First, 4 g Py-OMe was added to a 250 mL three-necked flask under the protection of nitrogen. After it was dissolved in 40 mL CH_2Cl_2 completely, the reaction mixture was kept in an ice water bath and then 8 mL BBr_3 , which was dissolved in 15 mL CH_2Cl_2 , was dropwise added into the stirred mixture at 0°C and stirred for 12 h at room temperature. Secondly, the mixture was cooled to 0°C again and 20 mL ice-water was dropwise added to hydrolyze any excess BBr_3 . Under stirring 2 h later, plenty of 20% sodium hydroxide was added until dissolved. Removed CH_2Cl_2 by reduced pressure distillation. In the end, via to adjust the pH value of the remaining liquid by hydrochloric acid to 6, white solid was separated out. After washed with water three times, The monomer, i.e., 2-(pyridin-4-yl)-1,4-benzenediol (Py-OH), was acquired and dried in a vacuum oven at 60°C for 24 hours.

4.2 Characterization of monomer

The chemical structure was identified via $^1\text{H-NMR}$ with DMSO-d_6 as the solvent. The internal reference was tetramethylsilane (TMS). As can be seen in Figure S2, the characteristic signal of the methoxyl group (Ar-OCH_3) was observed at approximately 3.75 ppm. After demethylation, this signal (3.75 ppm) disappeared, and two new singlets at approximately 8.91 and 9.12 ppm appeared, corresponding to the hydroxyl on the aromatic ring (Ar-OH). The results demonstrated that methyl had been taken off completely. Also, the proton signal of the aromatic ring (from 6.94 to

7.14) move to high field (from 6.64 to 6.82) as a result of the powerful electron-donating effect by hydroxyl groups. The signals of hydrogen in pyridine ring pendants were observed at about 8.55 and 7.54 ppm respectively. All signals were well assigned as shown. These results proved that the synthesis of Py-OH was successful.

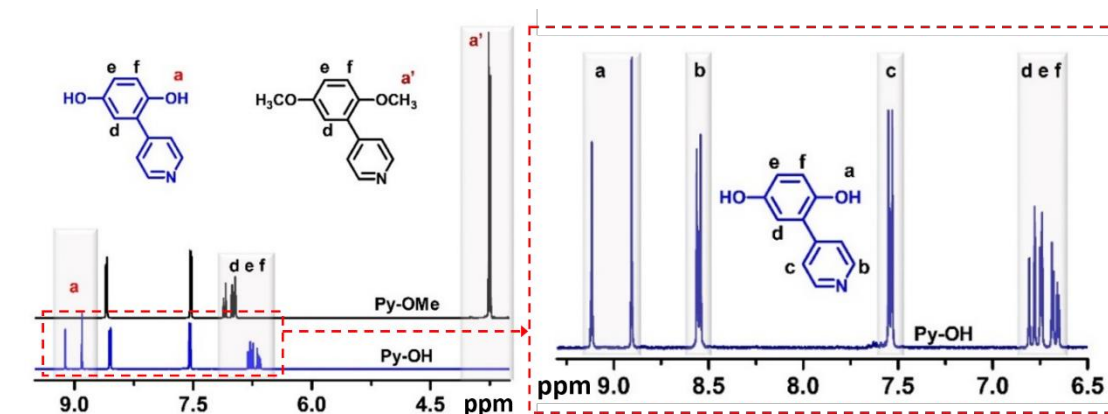


Figure S2. $^1\text{H-NMR}$ spectra (500 MHz, DMSO- d_6 , room temperature) of monomer.

Py-OMe

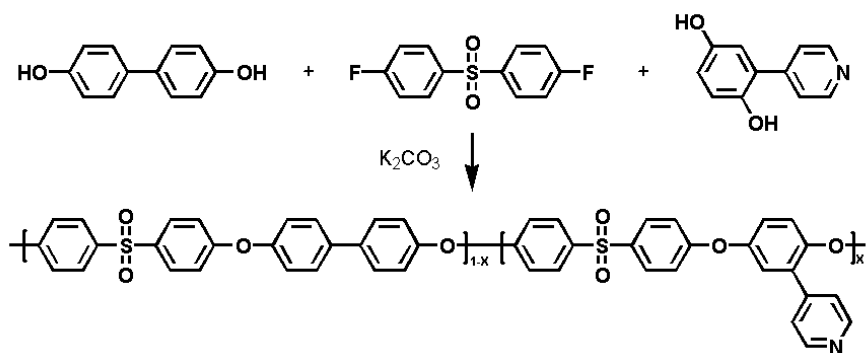
$^1\text{H NMR}$ (500 MHz, DMSO- d_6 , r.t.) δ 8.60 (dd, $J = 4.5, 1.6$ Hz, 2H), 7.53 (dd, $J = 4.4, 1.6$ Hz, 2H), 7.16 – 6.91 (m, 3H), 3.75 (d, $J = 6.9$ Hz, 6H).

Py-OH

$^1\text{H NMR}$ (500 MHz, DMSO- d_6 , r.t.) δ 9.12 (s, 1H), 8.91 (s, 1H), 8.55 (dd, $J = 4.5, 1.6$ Hz, 2H), 7.54 (dd, $J = 4.5, 1.6$ Hz, 2H), 6.72 (ddd, $J = 13.0, 11.6, 5.8$ Hz, 3H).

4.3 Synthesis of polymer

PPSU-Pyx was synthesized by an aromatic nucleophilic substitution reaction in a dipolar aprotic solvent. K_2CO_3 is used as base to ensure the nucleophilic ability of alkali metal hydroxides. The PPSu with any portion of pyridine group can be synthesized by controlling the monomer ratio accurately. A typical synthesis procedure of PPSU-Py60 is as follows:



Scheme S2. Synthesis of PPSU-Pyx

A 100mL three-necked round-bottom flask equipped with a mechanical stirrer, a nitrogen inlet with a thermometer, and a Dean–Stark trap with a condenser, was charged with 1.12 g Py-OH, 0.74 g 4,4'-biphenol, 2.54 g 4,4'-difluorodiphenyl sulfone, 1.5 g anhydrous K₂CO₃, 20 ml tetramethylene sulfone and 15 mL toluene. The mixture was stirred at room temperature for 10 min under argon atmosphere and then heated at 150°C for 3 h until the water was removed by azeotropic distillation with toluene. After the toluene was removed completely, the mixture was heated at 210°C for 6 h. Then the polymerization was complete and the viscous solution was poured into water. A blender was used to pulverize the flexible threadlike polymer. After being washed with hot deionized water and ethanol several times and dried under vacuum at 80°C for 20 h. 4 g pure polymer was obtained (yield 90%).

4.4 Characterization of co-polymer PPSU-Py.

As shown in Figure S3, the chemical structures of PPSU-Pyx were identified via ¹H-NMR with DMSO-d₆ as the solvent. All signals were well assigned.

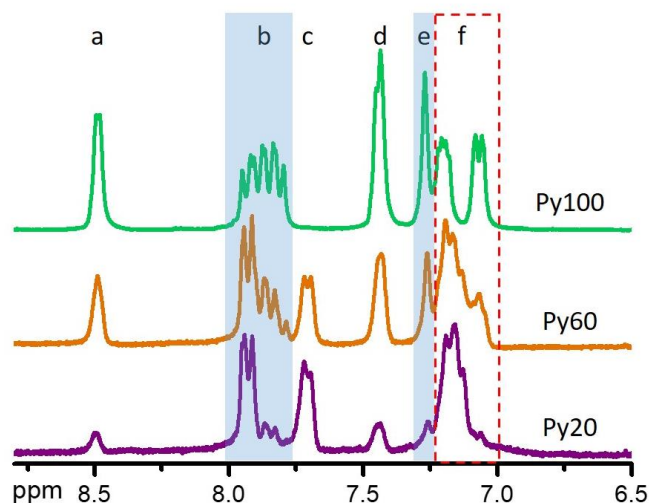


Figure S3. ^1H -NMR spectra (500 MHz, DMSO- d_6 , room temperature) of PPSU-Pyx.

The spectra showed clear trends with changing the content of pyridine groups. The integral ratio of the proton signal in the pyridine pendants around nitrogen at 8.5 ppm (signal a) and the proton signal in the aromatic ring around sulfone between 8.05 to 7.75 ppm (signal b) are, respectively, 0.1, 0.3, 0.5 (from top to bottom). On the basis of these, the molar percentage of the pyridine group pendants in PPSU-Pyx were calculated by $2a/b$ to be 20 %, 60 %, 100 % (from top to bottom). This proved that copolymers with different percent content of pyridine groups were synthesized

Py20

^1H NMR (500 MHz, DMSO- d_6 , r.t.) δ 8.50 (s, 2H), 7.89 (dd, $J = 24.0, 10.3$ Hz, 20H), 7.72 (s, 16H), 7.44 (s, 3H), 7.26 (s, 2H), 7.24 - 7.01 (m, 36H).

Py60

^1H NMR (500 MHz, DMSO- d_6 , r.t.) δ 8.49 (s, 6H), 8.05-7.77 (m, 20H), 7.71 (d, $J = 7.1$ Hz, 8H), 7.43 (s, 9H), 7.26 (s, 6H), 7.24 - 6.99 (m, 28H).

Py100

^1H NMR (500 MHz, DMSO- d_6 , r.t.) δ 8.49 (s, 2H), 8.03 - 7.72 (m, 4H), 7.44 (d, $J = 4.8$ Hz, 3H), 7.27 (s, 2H), 7.14 (dd, $J = 39.2, 5.6$ Hz, 4H).

5. Inherent viscosity of PPSU-Pyx

According to the viscosity theory of polymer solution, in extremely dilute solution, the inherent viscosity (η_{sp}) of polymer is close to its characteristic viscosity, and can be calculated by the following formula:

$$\eta_{sp} / c = \frac{\ln\left(\frac{t}{t_0}\right)}{c}$$

The inherent viscosity of PPSU-Pyx was measured by a Ubbelohde viscometer, with 0.1 g samples dissolved in 20 mL of DMAc at 25°C. As can be seen in Table S2, the inherent viscosities have no significant difference and means similar high molecular weight of PPSU-Pyx were synthesized successfully.

Table S2. Inherent viscosity of the PPSU-Pyx

PPSU-Pyx	Py20	Py60	Py100
Inherent viscosity (dL/g)	0.66	0.61	0.59

6. Nitrogen adsorption-desorption

Nitrogen adsorption-desorption (BET) was employed to analyze the pore size distribution of the prepared membranes. The result is similar to the results obtained by TEM image analysis.

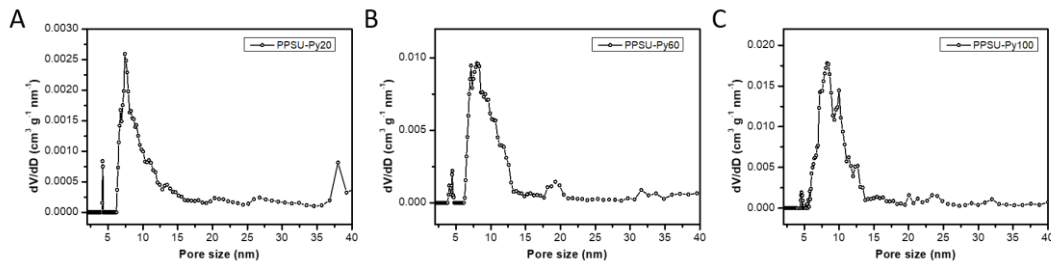


Figure S4. Pore size distribution of membranes PPSU-Py20, PPSU-Py60 and PPSU-Py100 measured by BET, respectively.

7. Numerical simulation

Since the 3D porous model is too complicated to build, for simplicity we hereby use a 2D model to gain insight into the ion transport mechanism. As for our PPSU-Py

membranes, no ionic current rectification phenomena exist, indicating the 3D pore structures inside the membrane are symmetric. So here, the simple model is built based on this as below (Figure S5).

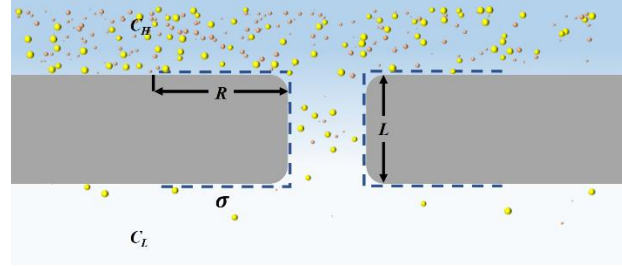


Figure S5. Schematic illustration of the 2D simulation model based on PNP theory.

Two reservoirs with the size of $8 \mu\text{m} \times 2 \mu\text{m}$ were separated by a nanopore. the surface charge density on the inner pore wall and outer membrane surface were σ , both of which were set to 0.06 C/m^2 . The transmembrane concentration difference $C_H | C_L$ was set to $100 | 1 \text{ mM}$. The pore size was fixed at 8 nm . The lengths of nanopore (L), namely the thickness of the films, were set at 2 nm , 200 nm and 500 nm . R is the length of charged area outside the orifice, which is inversely proportional to the porosity, and is set from 10 nm to 1000 nm .

The transmembrane ionic transport is presumed to be governed by the surface charge. The ion transport through the nanopore can be dominated by the Poisson and Nernst-Planck (PNP) equations at equilibrium

$$\nabla^2 \varphi = -\frac{\rho}{\epsilon_0 \epsilon_r}$$

$$J_i = -D_i \left(\nabla c_i + \frac{Z_i F c_i}{k_B T} \nabla \varphi \right)$$

Where ϵ_0 , ϵ_r , F , k_B , T are the vacuum permittivity, relative permittivity of water, Faraday constant, Boltzmann constant, temperature, respectively. And φ , ρ , J_i , D_i , c_i , Z_i are the local electrical potential, local charge density, local current density, diffusion coefficient, local ion concentration, valence of ionic species i , respectively. System work in steady state.

$$\nabla J_i = 0$$

The ionic current through the nanopore can be calculated

$$I_i = \int_S FZ_i J_i dS$$

The anion transference number t_n is then

$$t_n = \frac{|I_n|}{|I_n| + |I_p|}$$

Simulation results were shown in Figure S6. For long nanopores ($L > 200$ nm), the ionic transfer number and the diffusion current are dominated by the surface charges on the nanopore wall and stayed almost constant with respect to the length of charged area outside the orifice of long nanopores. Only at very high porosity, the interaction between pores can occur, the concentration polarization zone tends to overlap each other (Figure S6B). Nonetheless the decline of electric power generated was still limited, within 10% with $L = 500$ nm. As for the PPSU-Py membrane, the channel length is larger and the porosity is not high enough, so we believe the inter-pore ion depletion or aggregation impacted by the nearby pores has little influence to conductance and power density.

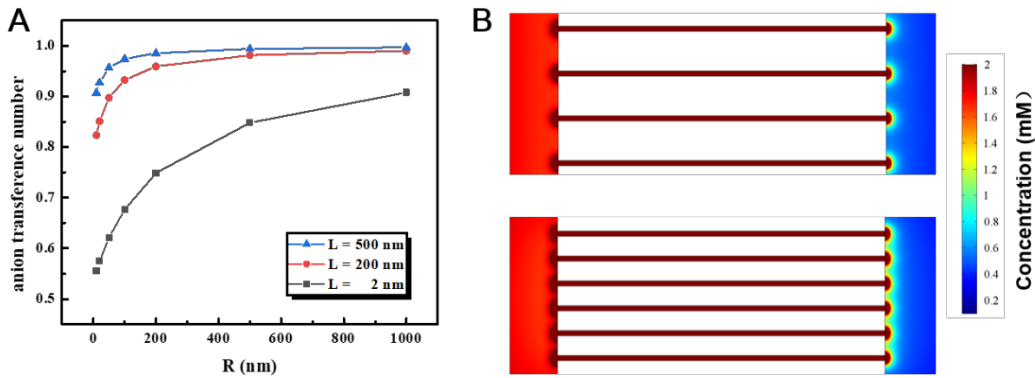


Figure S6. (A) Numerical simulation of the ionic transport performance. (B) Schematic illustrations of the ion distributions with different pore distances.

8. Ion selectivity and electrode calibration

The selectivity of the membrane is quantified in terms of transference number. Our PPSU-Py membrane behaves anion selectivity (t_n) which is calculated by equation (1)

$$t_n = \frac{1}{2} \left(\frac{E_{diff}}{\frac{RT}{zF} \ln \frac{\gamma_{C_H} c_H}{\gamma_{C_L} c_L}} + 1 \right) \quad (1)$$

Where t_n is the anion transference number; R, T, z, F, refer to the gas constant, temperature, valence charge and Faraday constant respectively; γ and c refer to ion activity coefficient and concentration; E_{diff} refers to the diffusion potential.

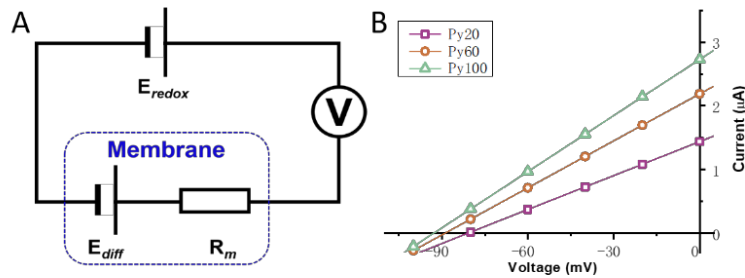


Figure S7. (A) The equivalent circuit diagram of the testing system. Only the E_{diff} is contributed by the membrane. (B) I–V curves of PPSU-Pyx membranes under artificial seawater (0.5 M NaCl) and artificial river water (0.01 M NaCl).

E_{diff} was tested by measuring the scanning I–V curves of PPSU-Pyx membranes under artificial seawater (0.5 M NaCl) and artificial river water (0.01 M NaCl). The equivalent circuit of the testing system is as shown (Figure S7). The intercept on the voltage axis (E_{open}) is contributed by the redox potential (E_{redox}) on the electrode and the diffusion potential (E_{diff}) from the membrane. R_m represents internal resistance of the PPSU-Py membrane.

Obviously, the diffusion potential (E_{diff}) can be calculated as $E_{diff} = E_{open} - E_{redox}$. An experimental method was used to subtract the contribution of the E_{redox} . In the same electrochemical experimental setup, the separator membrane was replaced by a nonselective silicon membrane containing a single micro-window in which case the measured voltage had contributions solely from the E_{redox} . This method could largely preclude the influence brought by other unexpected factors. The obtained E_{diff} are shown in Table S3. On this basis, anion selectivity (t_n) can be calculated.

From the experimental data, in the salinity gradient based on asymmetric seawater and river water, Py20, Py60 and Py100 showed high ionic selectivity, and with the increasing of functional groups, the membrane showed better selectivity, the t_n of Py100 was up to 0.773. This highly efficient selectivity would benefit the energy conversion process. The discussion above has been included in the revised manuscript as the reviewer requested.

Table S3. The anion transference number (t_n) of PPSU-Pyx membranes under artificial seawater (0.5 M NaCl) and artificial river water (0.01 M NaCl)

	PPSU-Py20	PPSU-Py60	PPSU-Py100
E_{open} (mV)	81	89	93
E_{diff} (mV)	42	50	54
t_n	0.712	0.753	0.773

9. Thermal stability of PPSU-Pyx

The thermal stabilities of the PPSU-Pyx were evaluated by thermogravimetric analysis (TGA) measurement under air atmosphere in the range of 80-700°C at a heating rate of 10°C min⁻¹. The polymers were kept in the TGA furnace at 120°C for 10 min before the analysis to completely remove the water.

As can be seen, before 400°C, which is the onset weight loss temperature, TGA curves were nearly flat. PPSU-Pyx all exhibited excellent thermal stability.

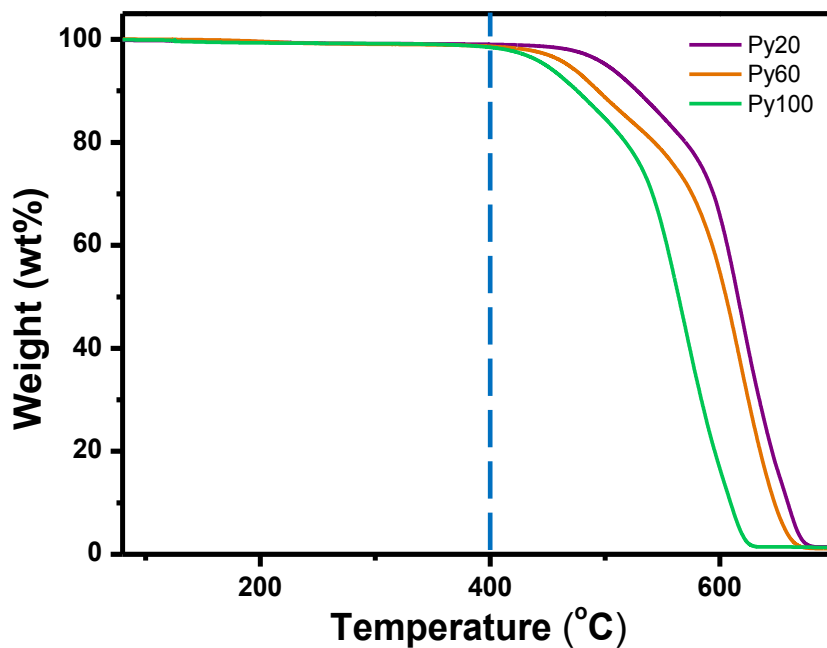


Figure S8. TGA curves of PPSU-Py20, PPSU-Py60 and PPSU-Py100.

10. Experimental setup

The experimental setup was built as shown in Figure 1D to study the power generation and ionic transport property of the membranes. The ionic current through the membrane was measured by a Keithley 6487 picoammeter (Keithley Instruments, Cleveland, OH). The transmembrane potential was provided by a pair of Ag|AgCl electrodes with equal electrolyte placed on the two sides of the membrane. Sweeping voltages from -2 V to 2 V was applied across the membrane. The membrane was fixed in the connector of two compartment as a separator. Electrolyte solutions were prepared with deionized water (18.2 M Ω ·cm, MilliQ).

Power generation devices were built by nanoporous membranes with unequal electrolyte placed on the two sides of the membrane. Artificial seawater (0.5 M NaCl) and artificial river water (0.01 M NaCl) were prepared to simulate the confluence of rivers and seas. The collected power is transferred to external circuit as supply an electronic load.